Inorganic Chemistry
Article

Inorg. Chem. **2009**, *48*, 8257–8262 **8257**
DOI: 10.1021/ic900762s

Two Variants of the $1/2[110]_p(203)_p$ Crystallographic Shear Structures: The Phasoid $Sr_{0.61}Pb_{0.18}(Fe_{0.75}Mn_{0.25})O_{2.29}$

Christophe Lepoittevin,[†,‡] Joke Hadermann,[‡] Sylvie Malo,*[,†] Olivier Pérez,[†] Gustaaf Van Tendeloo,[‡] and Maryvonne Hervieu[†]

[†]*Laboratoire CRISMAT-ENSICAEN, Bd du Maréchal Juin-14050 CAEN cedex, France, and* [‡]*EMAT, University of Antwerp, Groenenborgerlaan 171, B-2020 Antwerp, Belgium*

Received April 20, 2009

For the composition $(Sr_{0.61}Pb_{0.18})(Fe_{0.75}Mn_{0.25})O_{2.29}$, a new modulated crystallographic shear structure, related to perovskite, has been synthesized and structurally characterized by transmission electron microscopy. The structure can be described using a monoclinic supercell with cell parameters a_m = 27.595(2) Å, b_m = 3.8786(2) Å, c_m = 13.3453(9) Å, and β_m = 100.126(5)°, refined from powder X-ray diffraction data. The incommensurate crystallographic shear phases require an alternative approach using the superspace formalism. This allows a unified description of the incommensurate phases from a monoclinically distorted perovskite unit cell and a modulation wave vector. The structure deduced from the high-resolution transmission electron microscopy and high-angle annular dark-field−scanning transmission electron microscopy images is that of a $1/2[110]_p(203)_p$ crystallographic shear structure. The structure follows the concept of a phasoid, with two coexisting variants with the same unit cell. The difference is situated at the translational interface, with the local formation of double (phase **2**) or single (phase **1**) tunnels, where the Pb cations are likely located.

Introduction

The "ABO_3" perovskite structures are well-known to accommodate a large variety of structural modifications.[1,2] A huge amount of work has been devoted to the study of the chemical and physical properties associated with their flexibility in oxygen nonstoichiometry (ABO_{3-x}), but also in A-site cation deficiency (A_xBO_3), for which the octahedral framework of the nonstoichiometric A-site cation remains theoretically unchanged, down to $x = 0$ in the ReO_3-type structure. However, the intermediate value $x = 0.75$ is often considered as the limit of the "deficient perovskites" ($1 \geq x > 0.75$).

The Sr-based ferrites are exceptionally rich systems, especially by the existence of the oxygen-deficient perovskites $SrFeO_{3-y}$,[3−12] in which iron atoms can adopt a IV, V, or VI coordination. Sr deficiency in Sr_xFeO_{3-y} can be described by the formation of complex $[Fe_2O_{2.5-\varepsilon}]_\infty$ double layers in the perovskite matrix, up to the formation of an ordered phase for $x = 2/3$, corresponding to the composition $Sr_{2/3}FeO_{2.17}$ or $Sr_4Fe_6O_{13-\delta}$.[13−15] The structure refinements carried out in a 4D formalism[16] showed that, along $\vec{c}$, one perovskite-type slice $[SrFeO_3]_\infty$ alternates with one complex $[SrFe_2O_{3-\varepsilon}]_\infty$ slice related to a triple rock salt-type block. In the intermediate complex $[Fe_2O_{2.5-\varepsilon}]_\infty$ double layer, iron cations exhibit three types of coordination: tetragonal pyramids, trigonal bipyramids, and monocapped tetrahedra. The intergrowth of

*To whom correspondence should be addressed. E-mail: sylvie.malo@ensicaen.fr.

(1) Galasso, S. *Structure, Properties and Preparation of Perovskite Type Compounds*; Pergamon Press: Oxford, U. K., 1969.
(2) Mitchell, R. H. *Perovskites, Modern and Ancient*; Almaz Press: Thunder Bay, ON, Canada, 2002.
(3) Bertaut, E. F.; Blum, P.; Sagnieres, A. *Acta Crystallogr.* **1959**, *12*, 149–159.
(4) Marezio, M.; Remeika, P.; Chenavas, J; Joubert, J. C. *J. Solid State Chem.* **1985**, *58*, 243–252.
(5) Takeda, Y.; Kanno, K.; Takada, T.; Yamamoto, O.; Takano, M.; Nakayama, N.; Bando, Y. *J. Solid State Chem.* **1986**, *63*, 237–249.
(6) Grenier, J. C.; Pouchard, M.; Hagenmuller, P. *Struct. Bonding* (*Berlin*) **1981**, *47*, 1–25.
(7) Grenier, J. C.; Ea, N.; Pouchard, M; Hagenmuller, P. *J. Solid State Chem.* **1985**, *58*, 243–252.
(8) Takano, M.; Okita, T.; Nakayama, N.; Bando, Y.; Takeda, Y.; Yamamoto, O.; Goodenough, J. B. *J. Solid State Chem.* **1988**, *73*, 140–150.
(9) Hodges, J. P.; Short, S.; Jorgensen, J. D.; Xiong, X.; Dabrowski, B.; Mini, S.; Kimball, C. W. *J. Solid State Chem.* **2000**, *151*, 190–209.
(10) Greaves, C.; Jacobson, A. J.; Tofield, B. C.; Fender, B. E. F. *Acta Crystallogr.* **1975**, *B31*, 641–646.
(11) Takeda, T.; Yamaguchi, Y.; Watanabe, H. *J. Phys. Soc. Jpn.* **1972**, *33*, 967–969.
(12) D'Hondt, H.; Abakumov, A. M.; Hadermann, J.; Kalyuzhnaya, A. S.; Rozova, M. G.; Antipov, E. V.; Van Tendeloo, G. *Chem. Mater.* **2008**, *20*, 7188–7194.
(13) Kanamuru, F.; Shimada, M.; Koizumi, M. *J. Phys. Chem. Solids* **1972**, *33*, 1169–1171.
(14) Mellenne, B.; Retoux, R.; Lepoittevin, C.; Hervieu, M.; Raveau, B. *Chem. Mater.* **2004**, *16*, 5006–5013.
(15) Rossell, M. D.; Abakumov, A. M.; Van Tendeloo, G.; Pardo, J. A.; Santiso, J. *Chem. Mater.* **2004**, *16*, 2578–2584.
(16) Pérez, O.; Mellenne, B.; Retoux, R.; Raveau, B; Hervieu, M. *Solid State Sci.* **2006**, *8*, 431–443.

Published on Web 07/24/2009

one perovskite-type slice and one triple rock salt-type layer can be associated with a 2201-type structure,[17] and a large family of new materials, denoted Fe_A-$(n-1)2(m-1)m$, has been evidenced, with the members Fe_{Bi}-2212 and Fe_{Tl}-2234 associated with the formation of double and quadruple perovskite slices, respectively.[18,19] By doping the Sr site with Pb^{2+},[20] a solid solution is obtained (calculated to the equivalent composition $Sr_{0.55}Pb_{0.12}FeO_{2.17}$), whereas for a small lead excess $(Sr_{0.54}Pb_{0.17})FeO_{2.21}$, the formation of complex crystallographic shear (CS) planes is observed, with the stabilization of a "terrace structure"[21] described from the intergrowth of Fe_{Pb}-2201 and Fe_{Pb}-2212 structures. Besides the major steric role of the $6s^2$ lone pair of the $A = Bi^{3+}$ and Pb^{2+} cations, the combined effects of the valence and size (Ba^{2+} and Pb^{2+}) are indeed known to favor the formation of CS planes in similar layered ferrite structures.[22−27]

Recent studies of the Pb-rich ferrites in the "perovskite" $PbFeO_{2.5}$[28−30] highlight the role of the lone pair cation and evidence the existence of a large family of Pb-site-deficient perovskite-related compounds $Pb_{4m+3n}Fe_{4(m+n)}O_{10m+9n}$ with different $1/2[110](h0l)$ CS structures. It was shown that different CS structures can coexist in the same crystallite. The oxygen-deficient $Pb_{2/3}Sr_{1/3}FeO_{2.5}$[27] and $Pb_{0.5}Ba_{0.5}FeO_{2.5}$[31] frameworks have been proven to exhibit similar CS structures. The Pb−Mn−O compound $Pb_{0.9}MnO_{2.63}$, synthesized at 880 °C under 7.8 GPa, also exhibits a crystallographic shear structure, of the type $1/2[110]_p(704)_p$.[32] All structures are characterized by the formation of six-sided tunnels where two Pb^{2+} cations are located. However, in $Pb_{0.9}MnO_{2.63}$, the interface induces a translation by $1/4a_p\sqrt{2}$ along $[\bar{1}10]_p$ between two perovskite blocks and an elongation of the tunnels along $[100]_p$, whereas in the $Pb_{4m+3n}Fe_{4(m+n)}O_{10m+9n}$ structures, the perovskite blocks and the long diagonal of the tunnels are aligned along $[110]_p$. An overview of the reported members and of their structure determination from transmission electron microscopy (TEM) can be found in ref 33.

In order to understand the role played by the different cations in the formation of the crystallographic shear structures in the Sr-rich part of the ferrites system, doping of the B cation has been investigated for a cationic ratio A/B in the range 2/3−4/5. For the composition $(Sr_{0.61}Pb_{0.18})(Fe_{0.75}Mn_{0.25})O_{2.29}$, a new modulated CS structure has been synthesized, characterized by a perovskite related structure but different from the undoped terrace structure.[21] It has been studied by transmission electron microscopy, and its transport properties were characterized. Its relation to the different CS structures associated with A-cation-deficient perovskites is discussed.

Experimental Section

The powder compound was prepared in a glovebox starting from the oxides PbO, SrO, Fe_2O_3, and Mn_2O_3, in order to stabilize trivalent Fe^{3+} and Mn^{3+} cations. SrO was initially prepared by decomposing $Sr(OH)_2 \cdot 8H_2O$ at 1100 °C and was kept stored at this temperature. The precursors, weighed in the stoichiometric ratio, are ground to obtain a homogeneous powder. The mixture was then pressed into bars, sealed in a silica tube, and heated at 1100 °C for 48 h at a heating rate of 1.5 °C/min and slow-cooled at the same rate.

The X-ray powder diffraction (XRPD) analyses were carried out at room temperature with a Philips diffractometer using Cu Kα radiation ($\lambda = 1.5418$ Å) in the range $10° \leq 2\theta \leq 110°$.

The structural study was carried out using TEM. A small amount of sample was crushed in an agate mortar containing *n*-butanol, and a droplet was deposited on a copper grid covered with a holey carbon film. The electron diffraction (ED) investigation was carried out with a JEOL 200 CX microscope. The high-resolution TEM (HRTEM) was carried out using a JEOL 4000EX operating at 400 kV. HRTEM images were simulated using the Mac Tempas software. Z-contrast images were obtained on a JEOL 3000F microscope equipped with a scanning transmission electron microscopy (STEM) unit and a high-angle annular dark-field (HAADF) detector.

The resistivity measurements were carried out using the four-probes method on a physical properties measurement system.

Results

The X-ray Powder diffraction (Figure 1) and electron diffraction studies show that the synthesis resulted in a new phase. The homogeneity of the sample and the cationic composition were determined by combining the ED and EDS analyses. The cationic ratios have been measured on numerous crystallites, leading to an average cation ratio Sr/Pb/Fe/Mn close to 17:5:21:7, that is, $(Sr_{0.61}Pb_{0.18})(Fe_{0.75}Mn_{0.25})O_{2.29\pm\varepsilon}$ calculated per perovskite unit; the standard deviation is estimated to be 3% for the transition elements and strontium and increases to 7% for lead.

The compound is an insulator at 300 K with a resistivity on the order of 5×10^5 Ω cm. This value is consistent with the behavior observed for the different phases related to the strontium-rich phases Fe_A-$(n-1)2(m-1)m$ of the different

(17) Raveau, B.; Michel, C.; Hervieu, M.; Groult, D. *Crystal Chemistry of High Tc Superconducting Copper Oxides*; Springer-Verlag: Berlin, 1991; Springer Series in Materials Science 15.
(18) Grebille, D.; Lepoittevin, Ch.; Malo, S.; Pérez, O.; Nguyen, N.; Hervieu, M. *J. Solid State Chem.* **2006**, *179*(12), 3849–3859.
(19) Lepoittevin, C.; Malo, S.; Nguyen, N.; Hébert, S.; Van Tendeloo, G.; Hervieu, M. *Chem. Mater.* **2008**, *20*, 6468–6476.
(20) Lepoittevin, C.; Malo, S.; Van Tendeloo, G.; Hervieu, M. *Solid State Sci.* **2009**, *11*, 595–607.
(21) Lepoittevin, C.; Malo, S.; Pérez, O.; Nguyen, N.; Maignan, A; Hervieu, M. *Solid State Sci.* **2006**, *8*, 1294–1301.
(22) Hervieu, M.; Michel, C.; Caldes, M. T.; Pham, A. Q.; Raveau, B. *J. Solid State Chem.* **1993**, *107*, 117–126.
(23) Hervieu, M.; Caldes, M. T.; Michel, C.; Pelloquin, D.; Raveau, B. *J. Solid State Chem.* **1995**, *118*, 357–366.
(24) Hervieu, M.; Pérez, O.; Groult, D.; Grebille, D.; Leligny, H.; Raveau, B. *J. Solid State Chem.* **1997**, *129*, 214–222.
(25) Pérez, O.; Leligny, H.; Baldinozzi, G.; Grebille, D.; Graafsma, H.; Hervieu, M.; Labbé, Ph.; Groult, D. *Phys. Rev. B* **1997**, *56*, 5662–5672.
(26) Allix, M.; Pérez, O.; Pelloquin, D.; Hervieu, M.; Raveau, B. *J. Solid State Chem.* **2004**, *177*, 3187–3196.
(27) Raynova-Schwarten, V.; Massa, W.; Babel, D. *Z. Anorg. Allg. Chem.* **1997**, *623*, 1048–1054.
(28) Abakumov, A. M.; Hadermann, J.; Bals, S.; Nikolaev, I. V.; Antipov, E.; Van Tendeloo, G. *Angew. Chem., Int. Ed.* **2006**, *45*, 6697–6700.
(29) Hadermann, J.; Abakumov, A. M.; Nikolaev, I. V.; Antipov, E. V.; Van Tendeloo, G. *Solid State Sci.* **2008**, *10*, 382–389.
(30) Abakumov, A. M.; Hadermann, J.; Van Tendeloo, G.; Antipov, E. V. *J. Am. Ceram. Soc.* **2008**, *91*(6), 1807–1813.
(31) Nikolaev, I. V.; D'Hondt, H.; Abakumov, A. M.; Hadermann, J.; Balagurov, A. M.; Bobrikov, I. A.; Sheptyakov, D. V.; Pomjakushin, V.; Pokholok, K. V.; Filimonov, D. S.; Van Tendeloo, G.; Antipov, E. V. *Phys. Rev. B* **2008**, *78*, 024426-1-11.
(32) Bougerol, C.; Gorius, M. F.; Grey, I. E. *J. Solid State Chem.* **2002**, *169*, 131–138.
(33) Van Tendeloo, G.; Hadermann, J.; Abakumov, A. M. Antipov, E. V. *J. Mater. Chem.* **2009**, *19*, 2660−2670.

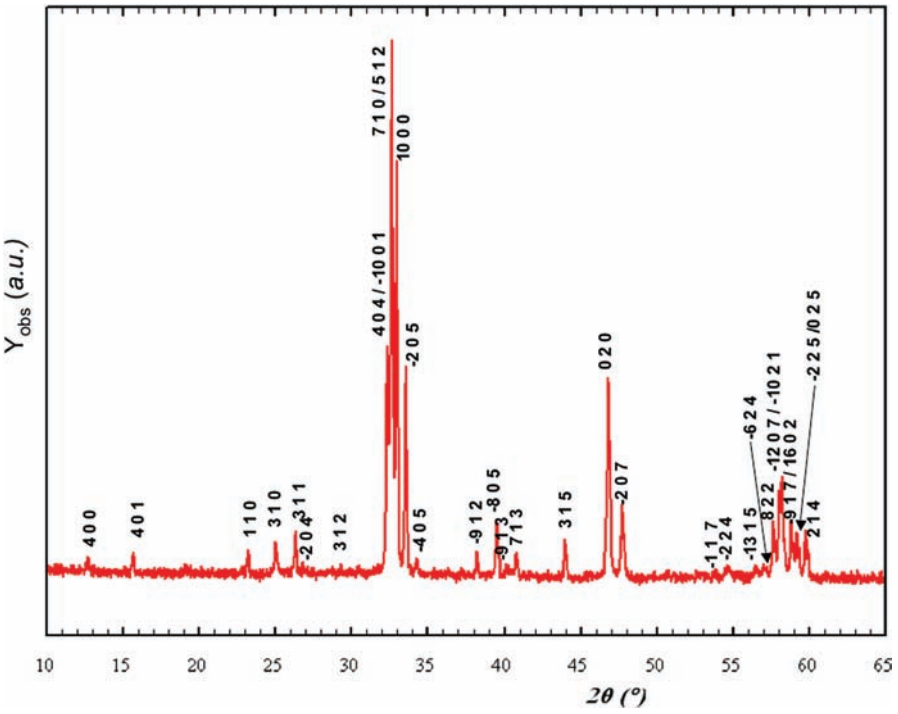

Figure 1. X-ray powder diffraction of $(Sr_{17}Pb_5)(Fe_{21}Mn_7)O_{64}$, $[(Sr_{0.61}Pb_{0.18})(Fe_{0.75}Mn_{0.25})O_{2.29}$; only the peaks corresponding to $I/I_0 > 2\%$ are indexed, I_0 representing the highest intensity observed].

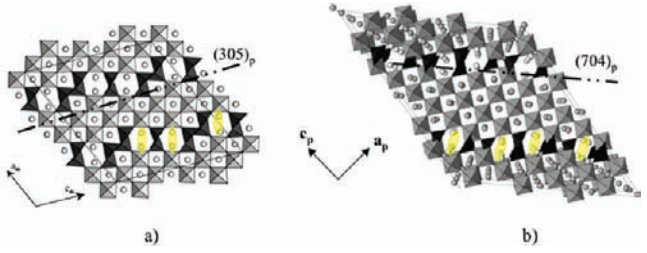

Figure 2. (a) The 1/2 [110](305)$_p$ structure of $Pb_{0.9}FeO_{2.4}$[28] and (b) the 1/2 [110](704)$_p$ structure of $Pb_{0.9}MnO_{2.63}$.[32]

systems (A = Ba, Pb, Bi, La),[18,20] which are characterized by a trivalent state of iron.

X-Ray and Electron Diffraction Techniques. The reciprocal space was reconstructed by tilting around several crystallographic axes. The ED patterns present large similarities to those reported for CS structures related to perovskite, such as the ferrite $Pb_{0.9}FeO_{2.4}$[28] (Figure 2a) and the manganite $Pb_{0.9}MnO_{2.63}$[32] (Figure 2b).

Out of these tilt series, a first example of a [010] ED pattern is given in Figure 3a. It shows features that are characteristic for such CS structures: a set of intense reflections, accompanied by weaker ones. An indexation, deduced from these tilt series, in agreement with the following monoclinic unit cell, $a_m \approx 27.6$ Å ($\approx 5a_p\sqrt{2}$), $b_m \approx 3.9$ Å, $c_m \approx 14.0$ Å ($\approx 13d_{(203)p}$), and $\beta \approx 101°$, can be proposed. The possible space groups compatible with the existence conditions observed for the reflections are *C*2, *Cm*, or *C*2/*m*. The cell parameters of the monoclinic supercell refined from XRPD patterns are $a_m = 27.595(2)$ Å, $b_m = 3.8786(2)$ Å, $c_m = 13.3453(9)$ Å, and $\beta_m = 100.126(5)°$. The corresponding reciprocal unit cell is indicated in Figure 3a by six monoclinic cells drawn around the origin. However such an interpretation is not totally satisfying because, depending

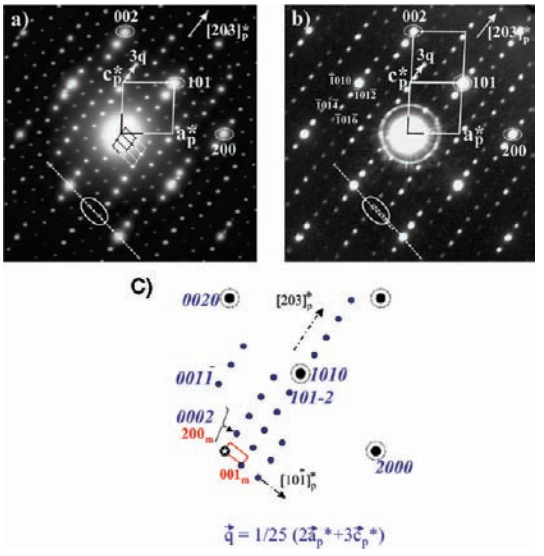

Figure 3. $(Sr_{0.61}Pb_{0.18})(Fe_{0.75}Mn_{0.25})O_{2.29}$. The intense reflections of the [010] ED patterns are indexed in a perovskite monoclinic subcell (drawn as a continuous line). (a) In this example, all of the reflections are indexed in a C-type monoclinic supercell with $a_m \approx 27.6$ Å ($\approx 5a_p\sqrt{2}$), $b_m \approx 3.9$ Å, $c_m \approx 14.0$ Å ($\approx 13d_{(203)p}$), and $\beta \approx 101°$ (drawn in dotted line). (b) Incommensurate pattern, associated with a modulation vector $q = 0.0787a_p^* + 0.01179c_p^*$. (c) Indexation of the pattern reproduced in part (a) considering the monoclinic supercell (red indices) or using four *hklm* indices (blue indices) with a commensurate *q* vector $q = 2/25a_p^* + 3/25c_p^*$. The two basic vectors $[203]_p^*$ and $[10\bar{1}]_p^*$ of the subcell are drawn.

on the selected area, losses of the periodicity are observed. Figure 3b illustrates this feature; along the $[10\bar{1}]_p$ direction, we observe a discontinuity in alignment of the reflections, which is not present in Figure 3a. A consequence of this aperiodicity is the impossibility of finding a supercell allowing a description of all diffraction patterns: a linear

combination of three basic vectors with integer coefficients does not permit the indexation of all reflections. The corresponding CS phases are clearly incommensurate, and only the superspace formalism allows a rigorous description of the patterns. Using an average monoclinic unit cell ($a_p \approx b_p \approx c_p \approx 3.9$ Å and $\beta_p \approx 87°$), identified considering the intense reflections (see Figure 3b), and introducing the modulation wave vector $\mathbf{q} = 0.0787a_p^* + 0.01179c_p^*$, each reflection can be indexed as follows: $ha_p^* + kb_p^* + lc_p^* + m\mathbf{q}$, with h, k, l, and m being integers (see Figure 3b). The systematic existence condition observed for the main and satellite reflections, $h + k + l + m = 2n$, is in agreement with the centering vector [1/2 1/2 1/2 1/2] and is compatible with the $I2/m(\alpha 0 \gamma)$ superspace group. Such a description of the reciprocal space can be successfully applied to the previous case described with the monoclinic supercell ($a_m \approx 27.6$ Å, $b_m \approx 3.9$ Å, $c_m \approx 14.0$ Å, $\beta \approx 101°$) but using a commensurate $\mathbf{q}$ vector: $\mathbf{q} = 2/25a_p^* + 3/25c_p^*$ with the same average monoclinic cell. Both indexations for this commensurate phase are schematically illustrated in Figure 3c. The major interest of the superspace approach is to provide a unified description of the reciprocal space for the complete CS structure family.

In the present contribution, we will mainly focus on the commensurate phase, of which the diffraction pattern is reproduced in Figure 3a.

HRTEM and HAADF-STEM Observations. Two [010] HRTEM images, carrying complementary information, recorded in the course of a focus series are reproduced in Figure 4. The images clearly illustrate the periodic formation of crystallographic shear planes in the perovskite structure, so that the present compound can be considered as a $1/2[110](203)_p$ CS structure. In Figure 4a, the high electron density zone positions are the darker ones (focus close to −190 Å), whereas in Figure 4b these are the brighter zones (focus close to −20 Å). The characteristic variations of the contrast at the level of the shear planes can be directly compared to those observed in the ferrite $Pb_{0.9}FeO_{2.4}$.[28] An important characteristic is observed at the interfaces: the alignment of the perovskites blocks and the long diagonal of the tunnels along $[101]_p$. This relative arrangement of the perovskite blocks attests to an extra displacement component denoted $R_1 = \varepsilon[001]_p$, with $\varepsilon \approx 1/3$.[29] Using the model of an ideal CS structure and based upon the comparison with the structure and images of $Pb_{0.9}FeO_{2.4}$, the dark dots on the HRTEM [010] image of Figure 4a are interpreted as cation positions forming perovskite blocks that are periodically translated in $(203)_p$ slices, while the dark zones between these slices and elongated parallel to $[110]_p$ can be associated with the six-sided tunnels surrounded by edge-sharing tetragonal pyramids. The HRTEM images show that the orientation of the crystallographic shear planes remains the same over large distances without suffering any deviation.

An interesting and important feature is the presence of two types of A cations with a significant difference in Z in the matrix (Pb = 82 and Sr = 38). HAADF STEM is the appropriate technique to study the preferential distribution of Pb in the cages of the framework. In so-called Z-contrast images, the intensity related to a column of atoms is proportional to Z^n $(1 < n < 2)$. The [010] HAADF STEM image (Figure 5a) exhibits rows of gray dots spaced by ≈5.5 Å along $[101]_p$ and $[\bar{1}01]_p$, associated with

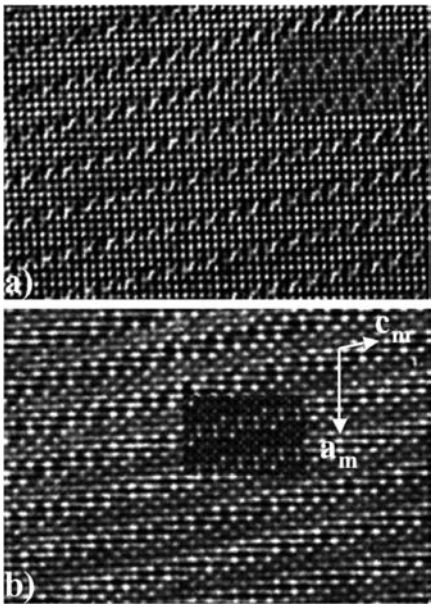

Figure 4. $(Sr_{0.61}Pb_{0.18})(Fe_{0.75}Mn_{0.25})O_{2.29}$ [010] HREM images of the same region at different defocuses. High electron density zones are dark in a and bright in b. The simulated images, calculated with the proposed models, are superimposed onto the experimental images.

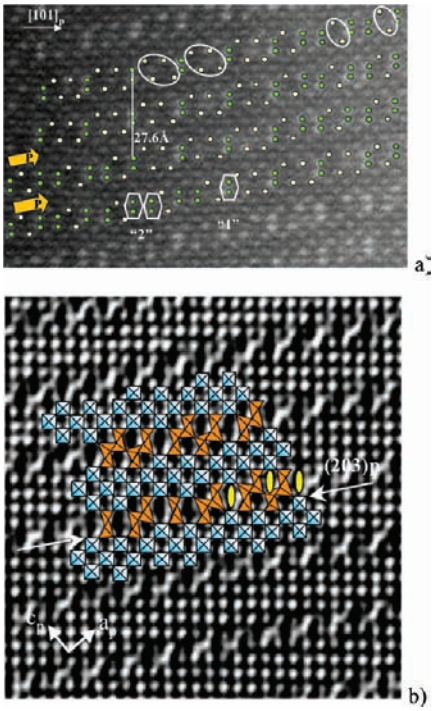

Figure 5. (a) [010] HAADF STEM image. The gray dots are associated with the projection of columns of A cations in the perovskite slices, while the brighter dots correspond to the six-sided tunnels. (b) Local structure obtained by overlaying the HRTEM image.

the projection of the columns of A cations in the perovskite slices (see the large yellow arrows). In between, dumbbells of brighter dots (parallel to $[101]_p$) and spaced by about 2.75 Å in projection are associated with the six-sided tunnels (labeled "H" hereinafter), and the brightness of the contrast suggests that they are filled in majority by lead cations (green dots in Figure 5a). The STEM image of Figure 5a also shows the existence of

five-sided tunnels (labeled "P" hereinafter) as well as double "H" tunnels, along $[\bar{3}02]_p$. Two single "P" tunnels are separated by four less bright dots, forming a lozenge (highlighted by a large ellipse), whereas two double "H" tunnels are separated by two gray dots (highlighted by a small ellipse). The combined information from the [010] HRTEM and HAADF STEM images, together with the help of the $Pb_{0.9}FeO_{2.4}$ $(1/2[110]_p(305)_p)$[28] and $Pb_{0.9}MnO_{2.63}$ $(1/2[110]_p(704)_p)$[32] structure analyses, provides a guide for the interpretation of the contrast of the present $1/2[110]_p(203)_p$ CS structure. The [010] HRTEM image in Figure 4a, where the high electron density positions are imaged as dark, has been used to draw a schematic model of the local structure in Figure 5b. The perovskite slice is clearly built up from octahedra periodically translated along a $(203)_p$ slice. In between these perovskite-type slices, the $(Fe/Mn)O_x$ polyhedra resulting from the shearing mechanism (drawn in the form of distorted pyramids shifted by $1/2[110]_p$) are corner-sharing and form long tunnels or distorted cages, where the Pb cations are most likely located; the Sr and possibly a minority of Pb cations occupy the perovskite cages.

The HAADF STEM images offer an understanding of the ordering arrangement, along $\vec{c}$, of the different distorted pyramids and, consequently, tunnels ("P" and "H") they manage at the level of the translational interfaces. Along the $[\bar{3}02]_p$ interface, the single and double "H" tunnels are distributed in alternating short sequences of a few species. Along $[101]_p$, single "P" tunnels tend to be aligned with single "P" tunnels at the adjacent interface or aligned with one of the double "H" tunnels (see vertical line in Figure 5a). The HAADF STEM images evidence that the perovskite blocks and the tunnels in the translation interfaces order according to two different patterns (**1** and **2** in Figure 6a), which have exactly the same monoclinic cell in 3D space ($a_m \approx 5a_p\sqrt{2}$, $b_m \approx 3.9$ Å, $c_m \approx 13d_{(203)p}$, and $\beta \approx 101°$) and the same *Cm* space group, in agreement with the refined parameters $a_m = 27.595(2)$ Å, $b_m = 3.8786(2)$ Å, $c_m = 13.3453(9)$ Å, and $\beta_m \approx 100°126(5)$.

The idealized models inferred from the above images are drawn in Figure 6b. One of these models, denoted phase **2,** is characterized by the presence of double "H" tunnels. The perovskite slice is built up of blocks of seven corner-sharing octahedra, translated along $[\bar{3}02]_p$ to form the perovskite $(203)_p$ slice. The adjacent perovskite slice is shifted by $(5a_p\sqrt{2}/2)$ along $[\bar{1}01]_p$ and $1/2\ \vec{b}_p$. The six-sided tunnels are surrounded by two octahedra, belonging to two adjacent perovskite slices, bordered by two structural B_2O_8 units made of two edge-sharing pyramids (B = Fe, Mn). These units are translated along $[\bar{3}02]_p$ so that the junction of two structural B_2O_8 units forms a block of four edge-sharing B_4O_{14} pyramids. A theoretical composition, $Pb_8Sr_{16}(Fe,Mn)_{26}O_{63}$, can be proposed for the structure **2** considering, with a simplifying aim, that Pb atoms are only located in the double "H" tunnels and that the pentagonal tunnels and perovskite cages are occupied by Sr atoms. The other model is characterized by the presence of single "H" tunnels and is denoted phase **1**. The perovskite slice is built up of blocks of six corner-sharing octahedra, and the seventh octahedron is now a pyramid that is part of a B_4O_{14} unit of the translation interface. Along $[\bar{1}01]$, the translation of the adjacent

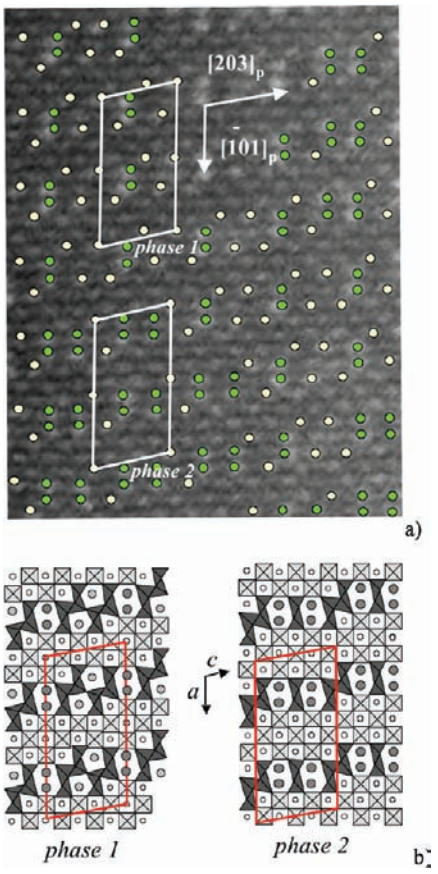

Figure 6. (a) HAADF STEM image showing the two types of patterns with exactly the same monoclinic cell. (b) Idealized models of the phases **1** and **2**.

perovskite slices is similar to that in the model **2**, $(5a_p\sqrt{2}/2)$ along $[\bar{1}01]_p$ and $1/2\vec{b}_p$. Two single "H" tunnels are separated by two B_4O_{14} units. The junction between two B_4O_{14} units creates pentagonal tunnels generating, together with the distorted perovskite cages, the lozenges observed in the STEM images. The theoretical composition of this cell **1** is $Pb_4Sr_{18}(Fe,Mn)_{28}O_{64}$, accounting for the same convention on the tunnels and cages' occupancy. Note that the two formulations involve a trivalent state of iron, in agreement with our conditions of synthesis.

Structure Analysis: A Phasoid? The models of the phases **1** and **2** (Figure 6b) deserve a thorough analysis because of the unusual existence of their common monoclinic cell. They are compared in Figure 7. The "perovskite blocks" only differ by one oxygen atom, making the seventh octahedron a pyramid (Figure 7a), and the translation interface has a common part, that is, one B_2O_8 unit, one tunnel, and one B_4O_{14} pyramid (Figure 7b).

The two frameworks **2** and **1** are built up as follows:

Framework "**2**": perovskite slices made of blocks of seven corner-sharing octahedra. Translation interface: two B_4O_{14} units and one B_2O_8 unit forming double "H" tunnels (Figure 6b)

Framework "**1**": Perovskite slices made of blocks of six corner-sharing octahedra+1 pyramid. Translation interface: two B_4O_{14} units forming single tunnels

The common features of the two models are illustrated in Figure 7c. The region, highlighted by the yellow

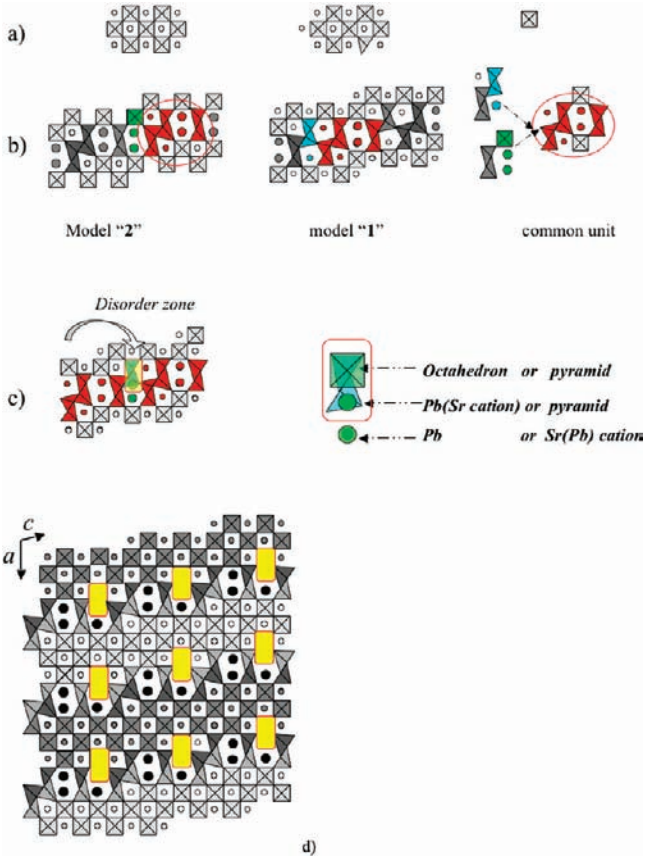

Figure 7. Comparison of models **1** and **2**: (a) in the "perovskite blocks" and (b) in the translational interface. (c) The difference lies in a critical zone (yellow rectangle) responsible for the two ordered nanophases. (d) The global structure can be written as $(Sr_{16}Pb_4)(Fe+Mn)_{26}M_4O_{64}$.

rectangle, is critical for the formation of the two models. If this zone is occupied by one octahedron (i.e., no oxygen vacancy) and two Pb ions (Figure 7b), the structure is that of model **2**; if it is occupied by two pyramids (i.e., oxygen vacancy) and one Sr(Pb) cation, the structure is that of model **1**. The above models have the same amount of cations, that is Pb + Sr + (Fe + Mn) = 50; the difference lies in the fact that one Fe pyramidal site (M = Fe) and one Pb site (M = likely Pb or Sr) can be exchanged in the highlighted zone. Considering the general formula $Sr_{16}Pb_4(Fe + Mn)_{26}M_4O_{64}$, the nature of the M cation is associated with one or the other structure in the common framework "$(Sr_{16}Pb_4)(Fe+Mn)_{26}$" (Figure 7d) built of the phases **1** and **2**.

These characteristics of closely related structures rather obey the concept of a phasoid, as described by Magneli.[34] This is illustrated in the STEM image (Figure 8) where the coexistence of both nanophases **1** and **2** is highlighted.

(34) Magneli, A. *Microsc. Microanal. Microstruct.* **1990**, *1*, 299–302.

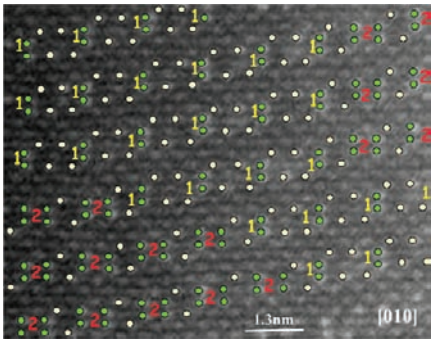

Figure 8. HAADF STEM image showing the coexistence of nanophases "**1**" and "**2**" (numbers refer to the structure models).

Concluding Remarks

This study reveals the existence of anion-deficient perovskite compounds in the Sr-rich part of the diagram. The investigation of the mechanism generating crystallographic shear structures in the Sr-rich ferrites confirms the major role played by the two cation ratios, A/B and Pb/Sr. Starting from the upper limit of the solid solution $Sr_{0.55}Pb_{0.12}FeO_{2.17}$ (A/B = (Sr + Pb)/(Fe) ≈ 0.67 and Pb/Sr + Pb = 0.18) with the structure type Fe_A-$(n-1)2(m-1)m$,[20] it appears that a small excess of lead (Pb/Sr + Pb ≥ 0.2) induces the formation of complex CS $1/2[110](hkl)_p$ structures[21] and that the stabilization of the six-sided tunnels requires a higher A/B cation ratio.

An interesting point in the present material is the existence of two structures, having a similar 3D unit cell but characterized by the presence of either single or double six-sided tunnels, denoted "H". These structures can be considered as two ordered nanostates of an average macroscopic structure $(Sr_{16}Pb_4)(Fe + Mn)_{26}M_4O_{64}$, with M = Pb or Sr and (Fe, Mn), and therefore the material can be considered a phasoid. The possible occupancy of the M sites by one of the four cations can be compared to different structural mechanisms observed in the terrace structures,[24,26,21] at the junction between the mixed rock salt-type [(Sr,A)O] layers (A is a lone pair cation, Bi^{3+} or Pb^{2+}) and the $[FeO_{2-x}]$ layers.

Finally, it is important to outline that the two models presented herein are associated with a sole monoclinic cell, with the commensurate **q** vector $\mathbf{q} = 2/25a_p^* + 3/25c_p^*$, and allow the structural mechanism of the average structure to be explained. However, keeping in mind that the ED investigation has evidenced local losses of the periodicity, the origins of the incommensurate modulated structures must be explained through the mechanism of the phasoid formation. The study of these nonstoichiometry mechanisms is in progress.

Acknowledgment. The authors acknowledge financial support from the European Union under the Framework 6 program under a contract for an Integrated Infrastructure Initiative, reference 026019 ESTEEM.